

Mechanically Excellent Nacre-inspired Protective Steel-Concrete Composite against Hypervelocity Impacts

Yong Mei

Institute of Defense Engineering, AMS, PLA,

Jinming Liu

Institute of Defense Engineering, AMS, PLA,

Yuan Cui

Institute of Defense Engineering, AMS, PLA,

Feng Li

Institute of Defense Engineering, AMS, PLA,

Xuke Tang

Beihang University

Miao Sun

Harbin Institute of Technology

Ruiqiang Chi

Harbin Institute of Technology

Yongbo Zhang*

Beihang University

Ao Zhang*

Institute of Defense Engineering, AMS, PLA,

Ke Chen* (✉ chenke0119@buaa.edu.cn)

Beihang University

Research Article

Keywords: Steel-concrete (SC), military defensive project, Hypervelocity Impacts

Posted Date: August 3rd, 2021

DOI: <https://doi.org/10.21203/rs.3.rs-745632/v1>

License: © ⓘ This work is licensed under a Creative Commons Attribution 4.0 International License. [Read Full License](#)

Abstract

Steel-concrete (SC) composite widely used in military defensive project is due to its impressive mechanical properties, long-lived service, and low cost. However, the growing use of hypervelocity kinetic weapons in the present war puts forward higher requirements for the anti-explosion and penetration performance of military protection engineering. Here, inspired by the special 'brick-and-mortar' (BM) structural feature of natural nacre, we firstly construct a nacre-inspired steel-concrete (NISC) engineering composite with 2510 kg/m^3 , possessing nacre-like lamellar architecture *via* a bottom-up assembling technique. The NISC engineering composite exhibits nacreous BM structural similarity, high compressive strength of 68.5 MPa, compress modulus of 42.0 GPa, Mohs hardness of 5.5, Young's modulus of 41.5 GPa, and shear modulus of 18.4 GPa, higher than pure concrete. More interestingly, the hypervelocity impact tests reveal the penetration capability of our NISC target material is obviously stronger than that of pure concrete, enhanced up to about 46.8% at the striking velocity of 1 km/s and approximately 30.9% at the striking velocity of 2 km/s, respectively, by examining the damages of targets, the trajectories, penetration depths, and residual projectiles. This mechanically integrated enhancement can be attributed to nacre-like BM structural architecture derived from assembling the special steel-bar framework-reinforced concrete platelets. This study highlights a key role of nacre-like structure design in promoting the enhanced hypervelocity impact resistance of steel-concrete composites.

Introduction

Concrete composite as one of inorganic materials has key role to society, including in civil building construction, mechanical engineering, and military facilities (*e.g.*, bulletproof walls and structure in nuclear power facilities, and the protective shelters of surface facilities) owing to its excellent formability, fire resistance, and durability¹⁻³. However, with the gradual emergence of variously advanced offensive hypersonic weapons (the striking velocity reaches possible up to 2 km/s), the penetration capability and destructive effect of projectiles have been greatly improved. Obviously, the impact resistance of traditional reinforced concrete structures such as steel-concrete armours has been not enough to satisfy with the protective requirements of these critical facilities⁴⁻⁶. Therefore, the exploitation of advanced protective steel-concrete (SC) materials and structures with light weight, robust mechanical performance, and excellent anti-penetration capability has become a main research in the field of shock resistance^{5,7}.

In nature, numerous shock-resistant, hierarchically heterogeneous biomaterials such as mollusk shells, bone, and mammalian tooth enamel comprise primarily some inorganic substances and are used for structural purposes⁸⁻¹². Among various types of biogenic forms of biominerals, the most popular example is probably mollusk shell with nacreous microstructural feature, where a 'brick-and-mortar' (BM) structure in nacreous layer comprised of 95 vol.% of platelets of inorganic aragonite (CaCO_3) and 5 vol.% of a protein (Fig. 1A)¹³⁻¹⁵. The impressive fracture toughness of natural nacre makes it one of the most widely studied biomaterials which can achieve a toughness orders of magnitude greater than either of its constituents^{8,16}, and meanwhile, the BM design strategy is a unique inspiration for numerous material scientists. Many researchers' groups have intelligently utilized the strategy to prepare various nacre-like hybrid composites including long fiber, thin films, and centimeter-sized bulk materials, which even obtain more outstanding mechanical properties compare with those of the nacreous layer¹⁷⁻²². Therefore, by understanding this advantage in the fascinating spatial structural heterogeneity of natural nacre, it will guide some new high-performance engineering composite materials which can be potentially applied in military facilities and civil building engineering. However, in spite of two decades of research effort, this nacre-inspired strategy mainly focuses on the preparation of small (centimeter)-sized nacre-like composite materials^{19,22,23}. Obviously, large-sized, nacre-inspired composite bulks have wider practical applications in military facilities in comparisons with small-sized composite bulks. With respect to concrete composite materials, although a number of protective SC composite barriers with various structural features have been developed in previous reported works^{4-7,24-26}, there is no example using this bioinspired designed strategy to create nacre-like high anti-penetration performance SC composite architectures.

In this work, inspired by the structural feature of natural nacre, we successfully construct large-sized, protective nacre-like steel-concrete (NISC) composite bulk targets with unique macroscopic lamellar architectures. Our approach is based on the precise

controlling assembly of steel framework-reinforced concrete building blocks on a pre-defined process routine to create architected nacreous macrostructure. During the construction process, we solve two critical challenges: developing the mechanically high-performance steel-meshed building blocks and optimizing the enhanced interfacial interactions between the adjacent lamellar building blocks in the NISC structures. Static mechanical tests reveal that our NISC composite materials achieve compressive strength of 68.5 MPa, compress modulus of 42.0 GPa, Mohs hardness of 5.5, Young's modulus of 41.5 GPa, and shear modulus of 18.4 GPa, greatly higher than the pure concrete. More importantly, based on the hypervelocity impact tests for examining the damages of targets, the trajectories, penetration depths, and residual projectiles, we demonstrate that the penetration capability of our NISC target material is obviously stronger than that of pure concrete, enhanced up to about 46.8% at the striking velocity of 1 km/s and approximately 30.9% at the striking velocity of 2 km/s, respectively. The unique mechanical combination can be due to the nacre-like BM structural architecture assembled from the special steel-bar framework-reinforced concrete platelet glued by a soft organic matrix. Predictably, the successful preparation of the large-sized, nacre-inspired SC composite materials will guide us to design and construct building construction and facilities satisfying the protective requirements.

Results

Design and assembly

Natural hard materials with the hierarchical heterogeneous structure can inspire new paths to construct some advanced materials with outstanding mechanical properties^{27,28}. We designed a protective NISC composite material that could embody a unique macroscopic lamellar architecture and a higher impact resistance capability or more excellent anti-penetration performance. As shown in Fig. 1B, the special steel-bar framework, which consisted of ordered quadrate patterns on the plane and an insertion of out-of-plane steel bar array with about 30 mm height, was first constructed by the welding process. These **soldering points** in the steel bar structural frame were sufficiently strong to withstand considerable impact without damage. Next, the steel bar framework was placed into a regular shuttering constructed with concrete placing and curing to form steel bar framework-reinforced concrete platelet as an ideal building block (Length × Width × Height (Dimension) = 300 mm × 300 mm × 50 mm), mimicking nacreous platelet. The dimension was chosen to create platelets with an aspect ratio of 6, which is slightly lower than the mineral platelets (10) in natural nacre^{8,16}. Furthermore, a steel framework-reinforced concrete platelet was assembled/glued on the top surface of staggered nacre-like arrangement by a ~5 mm silicone polymeric interlayer, in order to form the polymer-coated steel-concrete structural unit. An important step was to select the polymers with mechanical attributes similar to the interfaces in natural mollusk shell. Several polymers we tested in shear were too brittle (**leading to poor energy absorption**) and/or too strong (resulting in unwanted fracture of the glued layer). Silicone polymer material was eventually selected as the cross-linked interface material because of its relatively low strength, very high deformability in shear, strain hardening, and high energy absorption. Several framework-reinforced concrete platelets were laminated with ~5 mm thick polymeric interlayers. During the assembly, the framework-reinforced concrete platelets were carefully aligned so that the tablets formed a staggered nacre-like arrangement **analogous to** natural nacre¹³. Finally, the NISC target material with two different sizes (Dimension = 300 mm × 300 mm × 100 mm and 300 mm × 300 mm × 300 mm), could be obtained by the bottom-up assembly technique, named by NISC-100 and NISC-300, respectively. Clearly, the effect of macroscopic nacre-like architectural design on the mechanical properties will be reflected in superior rigidity of the NISC composite compared with conventional SC composite at the same overall geometric density, similar with the construction of the impact-resistant nacre-like super glass composite²⁷.

The whole preparation process of the NISC composite material is shown in Fig. 1C. We could observe that (from left to right): I) the unique steel bar framework was finely welded; II) the concrete was poured into the framework to form the steel framework-reinforced concrete platelet; III) the 5mm-thickness silicone polymer material was uniformly coated on the surface of the steel-concrete structural unit; IV) the NISC composite material was finally constructed to be applied as test target material, as shown in Fig. 1C. For the convenience of subsequent performance testing, these different types of target materials were packaged by home-made galvanized iron molds (see detailed in Supplementary Fig. 1).

Static mechanical performance

To prove the obvious validity of this nacre-inspired design strategy to construct the steel bar reinforced concrete material, the static mechanical responses of these concrete target materials with special sizes were studied first, as shown in Fig. 2 and Supplementary Table 1. Firstly, we can observe that the special specimen of the bulk concrete was deformed/broken by compressive tests (Fig. 2A). Obviously, the NISC target materials displays a better compressive mechanical performance compared with pure concrete. The compression stress of the NISC concrete material is about 68.5 MPa, which is about 32.0% higher than that of pure concrete (51.9 MPa). The value of compress modulus and Mohs hardness for the NISC composite material is ~42 GPa and ~5.5 GPa, respectively, clearly superior to that of the pure concrete (Fig. 2C). Bending tests further revealed that the NISC composite material achieved a better bending resistance capability in comparison with pure concrete. Compared to pure concrete, the maximum Young's modulus and shear modulus of the NISC composite material is clearly enhanced, up to ~41.5 GPa and ~18.4 GPa, respectively, superior to those of the pure concrete (36.6 ± 4.5 GPa and 15.6 ± 2.0 GPa).

Penetration of projectiles

The anti-penetration capabilities of the NISC composite targets were then systematically investigated by the hypervelocity impact tests to compare with that of the pure concrete under different striking velocities ($v = 1$ km/s and 2 km), as shown in Figs. 3-5, Supplementary Figs. 2-6 and Movies 1-3. Several shots of pointy ovoid-head steel projectiles (30CrMnSiA) penetrating into pure concrete and NISC targets are conducted. Firstly, the hypervelocity impact impressions on these target materials are observed with [optical photographs](#) and Movies (Figs. 3 and 4, and Supplementary Movies 1-3). Before the shots, the intact structural state of the target in the test equipment is shown in Fig. 3A-C. After the shots under a striking velocity of 1 km/s, there is a 5-mm [bullet hole](#) in the pure concrete. And a [crack propagation](#) along the bullet hole (the long crack cut through the whole target) to generate and the surficial concrete around the [bullet hole](#) also isn't destroyed, as displayed in Fig. 3D. Obviously, the localized damages occur on the impact surfaces of the concrete target, confirming that the dimensions of the target are large enough to neglect the boundary influences²⁹. To capture the shape and dimensions of impact craters more precisely, the silicone casting method was used to reconstruct the 3D crater and the projectile trajectory within the concrete, as shown in Fig. 3E. The damage of the pure concrete target, dimensions of crater, and a j-shaped crater followed by a cylindrical tunnel can be clearly observed. And then, the typical concrete targets were carefully cut along the penetration boreholes, the sectional views of the typical concrete targets are exhibited in Fig. 3F,G. We can observe that the projectile penetration forms a frustum-shaped crater followed by a cylindrical tunnel. [As we all know](#), the diameter of tunneling is consistent to that of projectile when the striking velocities are relatively low where the projectiles can be considered as rigid bodies³⁰. However, when the striking velocity was enhanced up to 2 km/s, the bullet hole in the pure concrete was obviously broaden, up to about 15 mm. Clearly, the tunneling diameter under is larger than that of the projectile, which further confirms the assumptions made by several researcher's groups^{29,30}. Several large [cracks propagate](#) around the bullet hole (these large cracks pass through the whole target), a [large area of](#) the surficial concrete around the [bullet hole](#) is seriously destroyed. And a heavy damaged state can be observed inside the concrete target. These results reveal that it isn't unaffordable for the common concrete against hypervelocity impacts.

Furthermore, after the penetration test, the pure concrete targets were carefully cut to recover the residual projectiles. Figure 3J presents the photographs of the 1 km/s and 2 km/s recovered projectile ($v_0 = 1$ km/s (top) and $v_0 = 2$ km/s (bottom)). Obviously, compared to the unfired projectile, the length and mass of residual projectile reduced a greater or lesser degree. The residual length and mass of 1 km/s recovered projectile (l_1, m_1) and 2 km/s recovered projectile (l_2, m_2) are 25.1 mm/5.48 g and 12.3 mm/3.56 g (see Table 1). The residual length and mass loss of the projectile at a striking speed of 2 km/s are [much more serious](#) than that at a striking velocity of 1 km/s. Quantitatively, the residual length and mass loss of the projectile change from 26.4 mm/5.76 g for unfired projectile to 25.1 mm/5.48 g for 1 km/s recovered projectile to 12.3 mm/3.56 g for 2 km/s recovered projectile, respectively. Correspondingly, when the initial velocity of projectiles is 1 km/s, the deformation of projectiles become evident, as shown in Fig. 3J. The blunted length of the recovered projectiles is 4.9%, while the relative mass

loss is also 4.9%. This regime indicates that the projectile is deformed but not eroded during the penetration process. When the initial velocity of projectile is 2 km/s, the relative mass loss is exacerbated and reach 38.2%. The mass loss and residual length of projectile increase and decrease with the rising of striking velocity, respectively. This regime is considered as eroding projectile penetration.

In contrast, we found that the impact impressions of the NISC composite target was clearly distinguished from that of pure concrete. After the NISC composite target was impacted under a striking velocity of 1 km/s, a **projectile** passed through the steel bar on the front NISC-100 target, leaving a small **bullet hole** in the pure concrete and a small crater; and a small **crack propagation** around the bullet hole. But these short cracks could not cut through the NISC target, and the surficial concrete around the **bullet hole** also was slightly damaged (Fig. 4A_I). In order to further study the damaged state inside the NISC-100 target at a striking velocity of 1 km/s, we observed the different layers (from the first layer to the third layer), as shown in Fig. 4A_{II-IV}. In first layer, a small area on the surface of the concrete was **peeled off**. However, the damage gradually reduces from second to third layers. On the back NISC-100 target (Fig. 4B_{I-IV}), we only observed a tiny piece of concrete around the **bullet hole**. The damage status has no obvious difference among these assembled layers.

However, after shooting at a striking speed of 2 km/s, the bullet hole in the front NISC-100 target became obviously larger than that at a striking velocity of 1 km/s. And several small **cracks propagate** around the bullet hole (these small cracks could not cut through the NISC target). Also, a 5 cm² **area of** the surficial concrete around the **bullet hole** was destroyed, as shown in Fig. 4C_I. With an increasing of the assembled layers, the damaged areas rapidly reduced (Fig. 4C_{II-IV}), clearly lower than that of the pure concrete (Fig. 3). However, on the back of the NISC-100 target (Fig. 4D), a 5 cm² area of surficial concrete around the **bullet hole** was peel off, accompanying with some **crack propagation** around the bullet hole (Fig. 4D_I). Although the crack could cut through the NISC target (see the different assembled layers), as shown in Fig. 4D_{II-IV}, the damage degree of the NISC target is notably smaller than that of the pure concrete. Based on the analysis of these damage morphologies, we consider that, our nacre-inspired steel-bar-reinforced concrete lamination can drastically enhance the damage tolerance of concrete materials under hypervelocity impacts.

In addition, to quantitatively estimate the impact resistance capability of these bioinspired composite targets, these important parameters (such as trajectory depth, penetration depth, residual length and mass of projectiles, impact crater area, and impact crater diameter) were summarized and compared in Fig. 5A-D, Table 1 and Supplementary Fig. 6. Generally, the impact resistance ability of the NISC target material was stronger than that of pure concrete material. For example, at a striking speed of 1 km/s, the trajectory depth, penetration depth, residual length and mass of the projectile, impact crater area, and impact crater diameter of the NISC target materials are 94.1 mm (NISC-300), 90.0 mm (NISC-300), 19.13 mm/4.94 g and 20.29 mm/5.01 g (NISC-100 and NISC-300), 1851/2154.99 mm² (NISC-100 and NISC-300), 48.55/73.08 mm (NISC-100 and NISC-300), respectively, obviously lower than those of the pure concrete (174.1 mm, 169.03 mm, 20.29 mm/5.01 g, 278.56 mm², and 73.81 mm). However, at a striking velocity of 2 km/s, the trajectory depth, penetration depth, residual length and mass of the projectile, impact crater area, and impact crater diameter of the NISC target materials are 102.3 mm (NISC-300), 97 mm (NISC-300), 10.00/9.11 mm and 2.96/2.72 (NISC-100 and NISC-300), 4018.27/3541.7 mm² (NISC-100/NISC-300), and 71.53/67.15 mm (NISC-100 and NISC-300), respectively, notably lower than those of the pure concrete (140.3 mm, 140.3 mm, 12.3 mm/3.56 g, 26028.98 mm², 182.05 mm). Simultaneously, we also found that the impact parameters of NISC-300 were lower than those NISC-100, suggesting that with increasing of the thickness of the bioinspired target, the impact resistance capability could be gradually enhanced.

Discussion

Combined the above static mechanics and anti-penetration capabilities of NISC composites, it can be confirmed that the nacre-like BM structural design is conducive to further enhance the load-bearing capability of NISC composite materials. Obviously, the optimal steel-concrete composite achieves an exceptional mechanical combination, which could potentially be utilized as an ideal target material. Actually, many researchers' groups have performed high strength steel (4340 steel, AerMet steel)

projectile penetration experiments on concrete targets, in which the strengths of targets of projectiles were ranged from 37.4 MPa to 65.6 MPa, corresponding striking velocities were ranged from 660 m/s to 1225 m/s, respectively³¹⁻³³. These projectiles were demonstrated to be eroded after the penetration tests, showing that the penetration process entered into the eroding stage for these projectiles/target integrations during the above striking velocity ranges³⁴. Generally, when the striking velocity of a penetration weapon is relatively low (*e.g.*, less than 0.8 km/s), the projectile deformation and failure can be negligible during the whole penetration process, therefore the penetration capability can be predicted through considering the projectile as a rigid body²⁹. However, with respect to our hypervelocity impact tests, the projectile must be blunted and even eroded owing to high pressure generated at the projectile/target interface, resulting in a drastic reduction of projectile penetration performance. Correspondingly, when the initial velocity of projectiles is 1 km/s, the blunted lengths of the recovered projectiles within NISC-100 and NISC-300 are 27.5% and 23.1%, respectively, while the relative mass losses are 14.2% and 13.0%. During the penetration process the projectile must be partially deformed but not eroded. Furthermore, when the initial velocity of projectile is 2 km/s, the blunted lengths and mass loss are visibly exacerbated, reach 62.1% and 65.5%, respectively. The residual length and mass loss of projectile increase and decrease with the rising of striking velocity, respectively. Similarly, during our penetration tests, the projectile occurs a large deformation and serious erosion, which can be considered as eroding projectile penetration. Besides, through comparing penetration depth of pure concrete with that of the NISC target material, we reckon that, the penetration resistance capability of the NISC target material can be enhanced up to about ~46.8% at the striking velocity of 1 km/s and ~30.9% at the striking velocity of 2 km/s, respectively. This large enhancement in the impact resistance of the bioinspired concrete material can be attributed to the co-effect of the special steel-bar framework-reinforced concrete design and nacre-like BM structural architecture.

As for theoretically predicting the penetration depth derived from high-speed projectile, Alekseevskii-Tate (A-T) model, as a 1D modified hydrodynamic model considering of contributions of projectile strength (Y_p) and target resistance (R_t), can be successfully used in the eroding projectile penetrations into metallic targets, where both projectile strength (Y_p) and target resistance (R_t) have explicit analytical expressions^{35,36}. In recent years, an extended dynamic spherical cavity expansion model (EDCEM) was presented by introducing a hyperbolic yield criterion and Murnaghan the equation of state (EOS) to successfully be applied to predict the one-dimension resistance of concrete-like materials for the one-dimension eroding projectile penetration problem²⁹. However, the eroding penetration model is only validated for concrete-like homogeneous composite materials. Unfortunately, for our nacre-like, heterogeneous SC composite materials there is still no available recognized model to predict the penetration depth of projectile under ultra-high velocity impacting tests. Therefore, the eroding penetration model for bioinspired heterogeneous SC composite to ultra-high projectile impact should be developed in the near future.

Table 1

Comparison for experimental results on different types of typical target materials after hypervelocity impacts under different striking velocities.

Target names	Density (kg/m ³)	Actual velocity (km/s)	Residual length (mm)	Residual mass (g)	Trajectory length (mm)	Penetration depth (mm)	Impact crater pixels (N)	Impact crater area (mm ²)	Equivalent diameter of impact crater (mm)
Concrete	2410	1.080	25.10	5.48	174.10	169.03	814809	4278.56	73.81
Concrete	2410	1.937	12.30	3.56	140.30	140.30	4873163	26028.98	182.05
NISC-100	2510	1.118	19.13	4.94	100.00	-	352504*	1851.00*	48.55*
NISC-100	2510	1.984	10.00	2.96	100.00	-	765239*	4018.27*	71.53*
NISC-300	2510	1.089	20.29	5.01	94.100	90.00	410396*	2154.99*	70.08*
NISC-300	2510	2.000	9.11	2.72	102.30	97.00	674483*	3541.71*	67.15*

*The first layer of the NISC target material.

Conclusion

By mimicking the special BM structural features of natural nacre in three dimensions and over large volumes we firstly construct a large-sized, excellent mechanical performance nacre-like SC composite barrier by assembling the steel framework-reinforced concrete building blocks glued by a soft silicone polymer in a simple bottom-up process. Compared to the homogeneous structure of pure concrete, the multiscale, hierarchical BM structural design with abundant hybrid interfaces can absorb larger amounts of mechanical energy, providing the composite barrier with higher strength, higher modulus, more excellent impact resistance, and stronger penetration resistance capability. The nacre-like SC composites also depict an architecture with relatively large size but with high order and periodicity, which is fully different from other previously reported nacre-like micro-nanocomposites^{17-20,24}. Finally, the macroscopic lamellar architecture and lamination fabrication methods are low-cost and relatively easy to implement into the large-scale production of impact-resistant nacre-like SC composite barriers for a wide range of potential applications, including civil building construction, mechanical engineering, and military facilities.

Materials And Methods

Materials and processing equipment

Silicate cement (PI52.5) was purchased from Xi'an Qinling Cement Factory. Silver sand (1.6-2.2 mm), high performance water-reducing agents, galvanized iron sheet (Thickness = 1.5mm), steel bar (R = 8 mm) was purchased from building material market. Silicone polymer material and curing agent were purchased from Shenzhen Youruiqi Technology Co. LTD. Besides, concrete mixers, cutting machines, forklifts, electric welding, and custom plastic molds also were used to prepare these target materials.

Experimental procedures

To prepare nacre-like steel concrete (NISC) composite target, we firstly constructed the steel-bar framework (Size: 280 mm × 280 mm × 25 mm), which is composed of regular square grids (Size: 70 mm × 70 mm) and regular steel columns (Long:

~10 mm) in the framework plane. Secondly, the well-mixed concrete (its proportional formula is shown in Table 2) was poured to form the steel-bar framework reinforced concrete structural unit. After the solidification of the concrete, a 5 mm-thickness polymeric silicone binder as soft phase was coated on the surface of the steel-bar framework reinforced concrete structural unit. Next, they were laminated together by stacking to form laminates with a total of 3-10 layers, being packaged by a home-made galvanized iron mold (see Supplementary Fig. 1A). Finally, the NISC composite targets with different sizes (300 mm × 300 mm × 100 mm and 300 mm × 300 mm × 100 mm) were successfully constructed by the bottom-up assembly method (Supplementary Fig. 1B,C). For comparison, pure concrete target with similar proportional composition was also prepared by the direct casting method (Supplementary Fig. 1D,E).

Static mechanical test

In the static mechanical test, the compressive tests were performed on a microcomputer controlled electro-hydraulic servo pressure tester. The testing method is in accordance with the standard of 'test methods for mechanical properties of ordinary concrete' (GB/T50081-2002). The working size of the specimens is shown in Table S1. The bending mechanical tests of specimens were performed on a multifunctional electro-hydraulic servo testing machine. The testing method referred to the standard of test methods for steel fiber reinforced concrete (JG/T472-2015).

Setup of hypervelocity impact test

As shown in Fig. 6, a two-stage light-gas gun system was employed to launch the projectiles. The system is mainly composed of a launching unit and a vacuum target chamber, as shown in Fig. 6A. The launching unit is used to accelerate the projectile to the target speed and launch projectile into the vacuum target chamber. The vacuum target chamber is used to place the target, in which projectile impacts the target. The diameters of the pump tube and the launching tube are 50 mm and 20 mm, respectively. Furthermore, its working principle is shown in Fig. 6B. Firstly, the N₂ gas is pushed into the sealed vessel by a compressor until to a designed pressure. Next, the value of N₂ vessel is opened and the plunger is accelerated in the pump tube which is filled with high-pressure hydrogen gas. At the end of the first-stage pump tube is a conical section, leading down to the second-stage 20 mm caliber launching tube that fires the projectiles. In this conical section, there is a rupture disk with a "+" pattern scored into the middle surface. When the hydrogen develops sufficient pressure to burst the scored section of rupture disk, the hydrogen flows through the hole and accelerates the projectiles with sabots located in the second-stage launching tube. After the projectiles are pulled out of the launching tube, the sabots are separated from the projectiles aerodynamically in the separation chamber filled with nitrogen gas (see some detailed process in SI)).

In the target chamber, the targets are placed with their impact surfaces perpendicular to the gun barrel. The striking velocity v is measured from a Photron SA5 high-speed camera placed in the projectile trajectory, as shown in Supplementary Fig. 2A. Before shooting, the trajectory position should be calibrated, and a moving distance in the image is obtained according to the actual calibration ruler length. The specific setup parameters are the aperture of 2,100,000 FPS and each frame of 1 μ s. The calibration image is exhibited in Supplementary Fig. 2B.

The [projectile](#) with sabots and its dimension parameter are shown in Fig. 7. The projectile is 30CrMnSiA, with a nominal density of 7.85 g/cm³, machining tolerance ± 0.01 mm, and staining treatment. During shooting at a striking velocity of 2 km/s, owing to the relatively large mass of the projectile and the insufficient carrying capacity of the sabots (the elastomer), the projectile would reverse attack the projectile during firing, resulting in substandard incident velocity and even scratching the gun tube. Therefore, a 2 mm × 10 mm titanium alloy gasket is added to reduce the damage of the elastomer. The diameter of the elastomer is 12.65-12.75 mm, so that the total mass of the whole projectile is slightly increased.

According to the condition of normal impact, upper support and rear support are provided for the relatively thick target materials, as shown in Supplementary Fig. 3A. The support doesn't provide prestress, but only plays a fixing role to prevent the target from turning over or moving. Besides, for testing and observing the thin target with thickness of 100 mm, we installed a

sighting board and a protective shield, as shown in Supplementary Fig. 3B. Owing to the large mass of the sighting board and protective shield, no additional support is used.

Table 2

The mix proportion of the concrete material.

Target	Content (ratio)			
	Cement	Sand	Aggregate	Water
Concrete	1.1	1	2.72	0.38

Declarations

Data availability

All data generated or analysed during this study are included in this published article (and its supplementary information files)

Acknowledgements

This work was supported by the National Natural Science Foundation of China (21905011).

Author contributions

Study design: Y.M., K.C., A.Z., Y.Z., M.S., and R.C. Experimental implementation: Y.M., M.S. Y.C., F.L., X.T., and R.C. Data analysis: K.C. and M.S. Data interpretation: K.C., Y.M., M.S., and R.C. Draft: K.C., Y.M., and Y.Z. Review and approval: all authors.

Funding

Open Access funding provided by the National Natural Science Foundation of China (21905011)

Competing interests

The authors declare no conflict of interest.

References

1. Kennedy, R. P. A review of procedures for the analysis and design of concrete structures to resist missile impact effects. *Nucl. Eng. Des*, **37** (2), 183–203 [https://doi.org/10.1016/0029-5493\(1975\)](https://doi.org/10.1016/0029-5493(1975)).
2. Adeli, H. *et al.* Local effects of impactors on concrete structures. *Nucl. Eng. Des*, **88** (3), 301–317 [https://doi.org/10.1016/0029-5493\(85\)90165-7](https://doi.org/10.1016/0029-5493(85)90165-7) (1985).
3. Gagg, C. R. Cement and concrete as an engineering material: An historic appraisal and case study analysis. *Eng. Fail. Anal*, **40**, 114–140 <https://doi.org/10.1016/j.engfailanal.2014.02.004> (2014).
4. Li, J. *et al.* An experimental and numerical study of reinforced ultra-high performance concrete slabs under blast loads. *Mater. Des*, **82**, 64–76 <https://doi.org/10.1016/j.matdes.2015.05.045> (2015).
5. Shao, R. *et al.* Experimental and numerical investigations of penetration resistance of ultra-high strength concrete protected with ceramic balls subjected to projectile impact. *Ceram. Int*, **45** (6), 7961–7975 <https://doi.org/10.1016/j.ceramint.2019.01.110> (2019).

6. Yankelevsky, D. Z. Resistance of a concrete target to penetration of a rigid projectile-revisited. *Int. J. Impact Eng*, **106**, 30–43 <https://doi.org/10.1016/j.ijimpeng.2017.02.021> (2017).
7. Shao, R. *et al.* Penetration resistance of ultra-high-strength concrete protected with layers of high-toughness and lightweight energy absorption materials. *Compos. Struct*, **185**, 807–820 <https://doi.org/10.1016/j.compstruct.2017.11.038> (2018).
8. Meyers, M. A. *et al.* Structural biological materials: critical mechanics-materials connections., **339** (6121), 773–779 <https://doi.org/10.1126/science.1220854> (2013).
9. Tertuliano, O. A. *et al.* The nanocomposite nature of bone drives its strength and damage resistance. *Nat. Mater*, **15**, 1195–1202 <https://doi.org/10.1038/nmat4719> (2016).
10. Yeom, B. *et al.* Abiotic tooth enamel. *Nature*, **543** (7643), 95–98 <https://doi.org/10.1038/nature21410> (2017).
11. Song, J. *et al.* Processing bulk natural wood into a high-performance structural material. *Nature*, **554** (7691), 224–228 <https://doi.org/10.1038/nature25476> (2018).
12. Amini, S. *et al.* The role of quasi-plasticity in the extreme contact damage tolerance of the stomatopod dactyl club. *Nat. Mater*, **14** (9), 943–950 <https://doi.org/10.1038/nmat4309> (2015).
13. Barthelat, F. *et al.* On the mechanics of mother-of-pearl: A key feature in the material hierarchical structure. *J. Mech. Phys. Solids*, **55** (2), 306–337 <https://doi.org/10.1016/j.jmps.2006.07.007> (2007).
14. Barthelat, F. *et al.* Toughness amplification in natural composites. *J. Mech. Phys. Solids*, **59** (4), 829–840 <https://doi.org/10.1016/j.jmps.2011.01.001> (2011).
15. Bouville, F. *et al.* Strong, tough and stiff bioinspired ceramics from brittle constituents. *Nat. Mater*, **13** (5), 508–514 <https://doi.org/10.1038/nmat3915> (2014).
16. Wang, J. *et al.* Layered nanocomposites inspired by the structure and mechanical properties of nacre. *Chem. Soc. Rev*, **41** (3), 1111–1129 <https://doi.org/10.1039/c1cs15106a> (2012).
17. Bonderer, L. J. *et al.* Bioinspired design and assembly of platelet reinforced polymer films., **319** (5866), 1069–1073 <https://doi.org/10.1126/science.1148726> (2008).
18. Munch, E. *et al.* Tough, bio-inspired hybrid materials., **322** (5907), 1516–1520 (2008).
19. Erb, R. M. *et al.* Composites reinforced in three dimensions by using low magnetic fields., **335** (5907), 199–204 <https://doi.org/10.1126/science.1164865> (2012).
20. Mao, L. B. *et al.* Synthetic nacre by predesigned matrix-directed mineralization., **354** (6308), 107–110 <https://doi.org/10.1126/science.aaf8991> (2016).
21. Xiao, C. *et al.* Total morphosynthesis of biomimetic prismatic-type CaCO₃ thin films. *Nat. Commun*, **8**, 1398 <https://doi.org/10.1038/s41467-017-01719-6> (2017).
22. Mouritz, A. P. *et al.* Review of applications for advanced three-dimensional fibre textile composites. *Part A Appl. Sci. Manuf*, **30** (12), 1445–1461 [https://doi.org/10.1016/S1359-835X\(99\)00034-2](https://doi.org/10.1016/S1359-835X(99)00034-2) (1999).
23. Veedu, V. P. *et al.* Multifunctional composites using reinforced laminae with carbon-nanotube forests. *Nat. Mater*, **5**, 457–462 <https://doi.org/10.1038/nmat1650> (2006).
24. Guan, Q. F. *et al.* Lightweight, tough, and sustainable cellulose nanofiber-derived bulk structural materials with low thermal expansion coefficient. *Sci. Adv*, **6** (18), eaaz1114 <https://doi.org/10.1126/sciadv.aaz1114> (2020).
25. Guan, Q. F. *et al.* An all-natural bioinspired structural material for plastic replacement. *Nat. Commun*, **11**, 5401 <https://doi.org/10.1038/s41467-020-19174-1> (2020).
26. Song, D. *et al.* Experimental investigation on the cellular steel-tube-confined concrete targets against projectile impact. *Int. J. Impact Eng*, **131**, 94–110 <https://doi.org/10.1016/j.ijimpeng.2019.05.004> (2019).
27. Yin, Z. *et al.* Impact-resistant nacre-like transparent materials., **364** (6447), 1260–1263 <https://doi.org/10.1126/science.aaw8988> (2019).

28. Paschalis, S. A. *et al.* Experimental and numerical study of the performance of ultra high performance fiber reinforced concrete for the flexural strengthening of full scale reinforced concrete members. *Constr. Build. Mater*, **186**, 351–366 <https://doi.org/10.1016/j.conbuildmat.2018.07.123> (2018).
29. Kong, X. Z. *et al.* Projectile penetration into mortar targets with a broad range of striking velocities: Test and analyses. *Int. J. Impact Eng*, **106**, 18–29 <https://doi.org/http://10.1016/j.ijimpeng.2017.02.022> (2017).
30. Rosenberg, Z. *et al.* The deep penetration of concrete targets by rigid rods-revisited. *Int. J. Protect. Struct*, **1** (1), 125–144 <https://doi.org/http://10.1260/2041-4196.1.1.125> (2010).
31. Frew, D. J. *et al.* The effect of concrete target diameter on projectile deceleration and penetration depth. *Int. J. Impact Eng*, **32** (10), 1584–1594 <https://doi.org/10.1016/j.ijimpeng.2005.01.012> (2006).
32. Liu, C. *et al.* Experimental and theoretical study on steel long-rod projectile penetration into concrete targets with elevated impact velocities. *Int. J. Impact Eng*, **138**, 103482 <https://doi.org/10.1016/j.ijimpeng.2019.103482> (2020).
33. Alavi Nia, A. *et al.* Analysis of resistance of concrete target against penetration of eroding long rod projectile regarding flow field around the projectile tip. *Int. J. Protect. Struct*, **57**, 36–42 <https://doi.org/10.1016/j.ijimpeng.2013.01.009> (2013).
34. Tate, A. A theory for the deceleration of long rods after impact. *J. Mech. Phys. Solids*, **15** (6), 387–399 [https://doi.org/10.1016/0022-5096\(67\)90010-5](https://doi.org/10.1016/0022-5096(67)90010-5) (1967).
35. Alekseevskii, V. P. Penetration of a rod into a target at high velocity. *Combust. Explo. Shock Waves*, **2**, 63–66 <https://doi.org/10.1007/BF00749237> (1966).
36. Tate, A. *et al.* Long rod penetration models—Part II. Extensions to the hydrodynamic theory of penetration. *Int. J. Eng. Sci*, **28** (9), 599–612 [https://doi.org/10.1016/0020-7403\(86\)90075-5](https://doi.org/10.1016/0020-7403(86)90075-5) (1986).

Figures

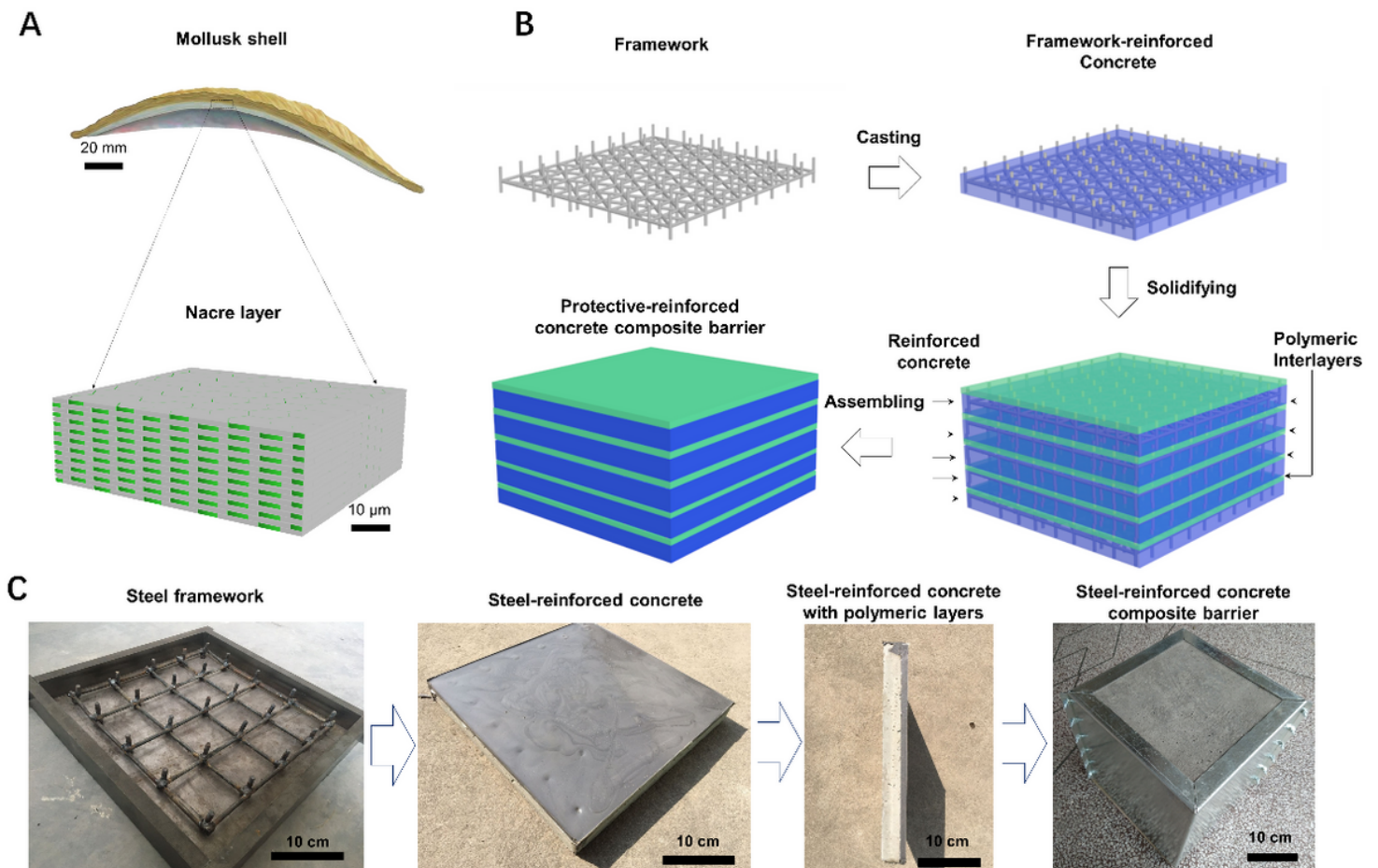


Figure 1

Design and fabrication of nacre-inspired steel-concrete (NISC) composite bulk target. (A) multiscale structural feature of natural mollusk shell, where nacreous layer made of mineral platelets glued by soft organic matrix, can obtain large deformation, utmost crack limit, and impressive impact energy absorbance by sliding of the micro-platelets. (B) Fabrication protocol schematic for the NISC composite bulk targets, referring to framework construction, pouring of concrete, and assembling process. (C) Digital photographs for the preparation process of the NISC target material. From left to right: steel framework, steel-reinforced concrete, steel-reinforced concrete with polymeric layer, and steel-reinforced composite target.

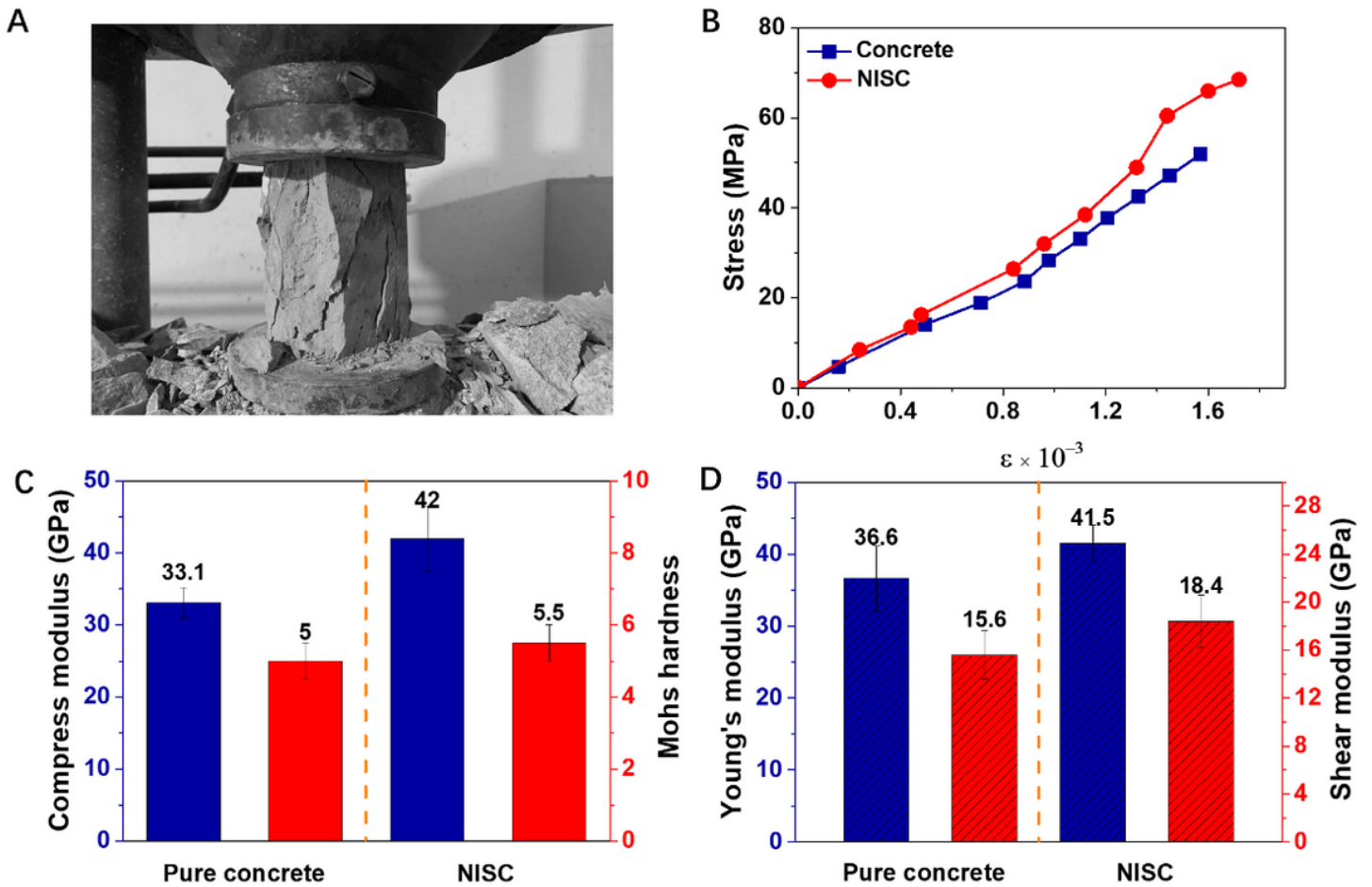


Figure 2

Comparison for the static mechanical properties of the NISC target and pure concrete materials. (A) Digital photograph of the target materials on a microcomputer controlled electro-hydraulic servo pressure tester, showing compressing process. (B) Stress-strain curves derived from the compression tests. (C) Compress modulus and Mohs hardness. (D) Young's modulus and shear modulus derived from the bending tests.

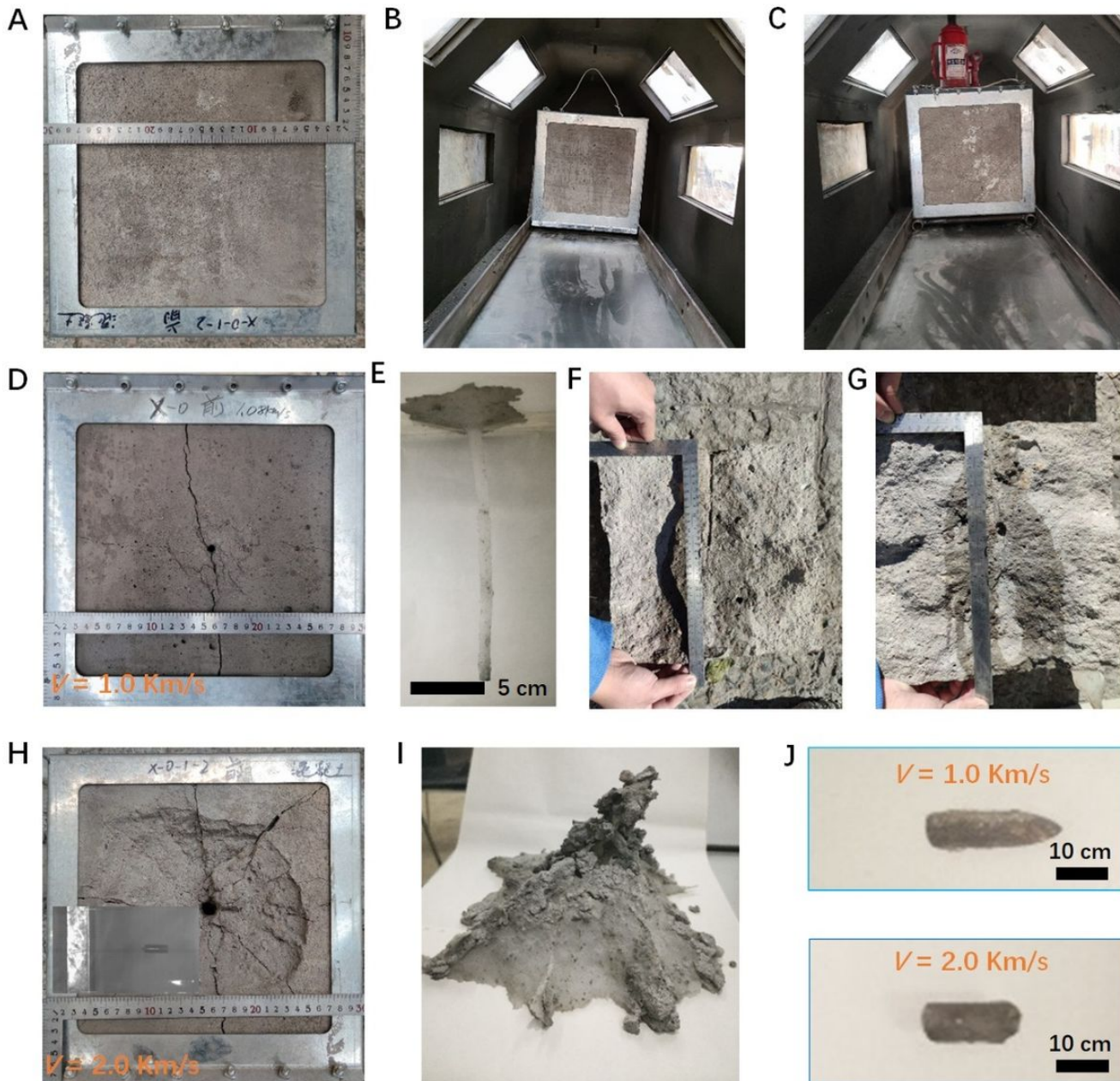


Figure 3

Photographs of typical target materials in the target chamber, its damage observation (including the cratering area, diameter and depth, and the trajectory) and eroding projectile, after the hypervelocity impact tests under different striking velocities ($v = 1 \text{ km/s}$, 2 km/s). (A) Photograph of the frontal concrete target. (B) Photograph of the frontal concrete target in the target chamber. (C) Photograph of the frontal concrete target fixed in the target chamber. (D) Photograph of the cratering of the frontal concrete target after a striking velocity of 1 km/s , showing a long crack along the bullet hole. (E) The j-shaped trajectory in the concrete target at $v = 1 \text{ km/s}$. (F, G) Cutting target (F) and the sectional view (G) of typical concrete target at $v = 1 \text{ km/s}$. (H) The cratering of the frontal concrete target at $v = 2 \text{ km/s}$. (I) Photograph of heavy damaged state inside the concrete target at $v = 2 \text{ km/s}$. (J) The morphologies of the residual projectile after the penetration under $v = 1 \text{ km/s}$ (top) and 2 km/s (bottom), respectively.

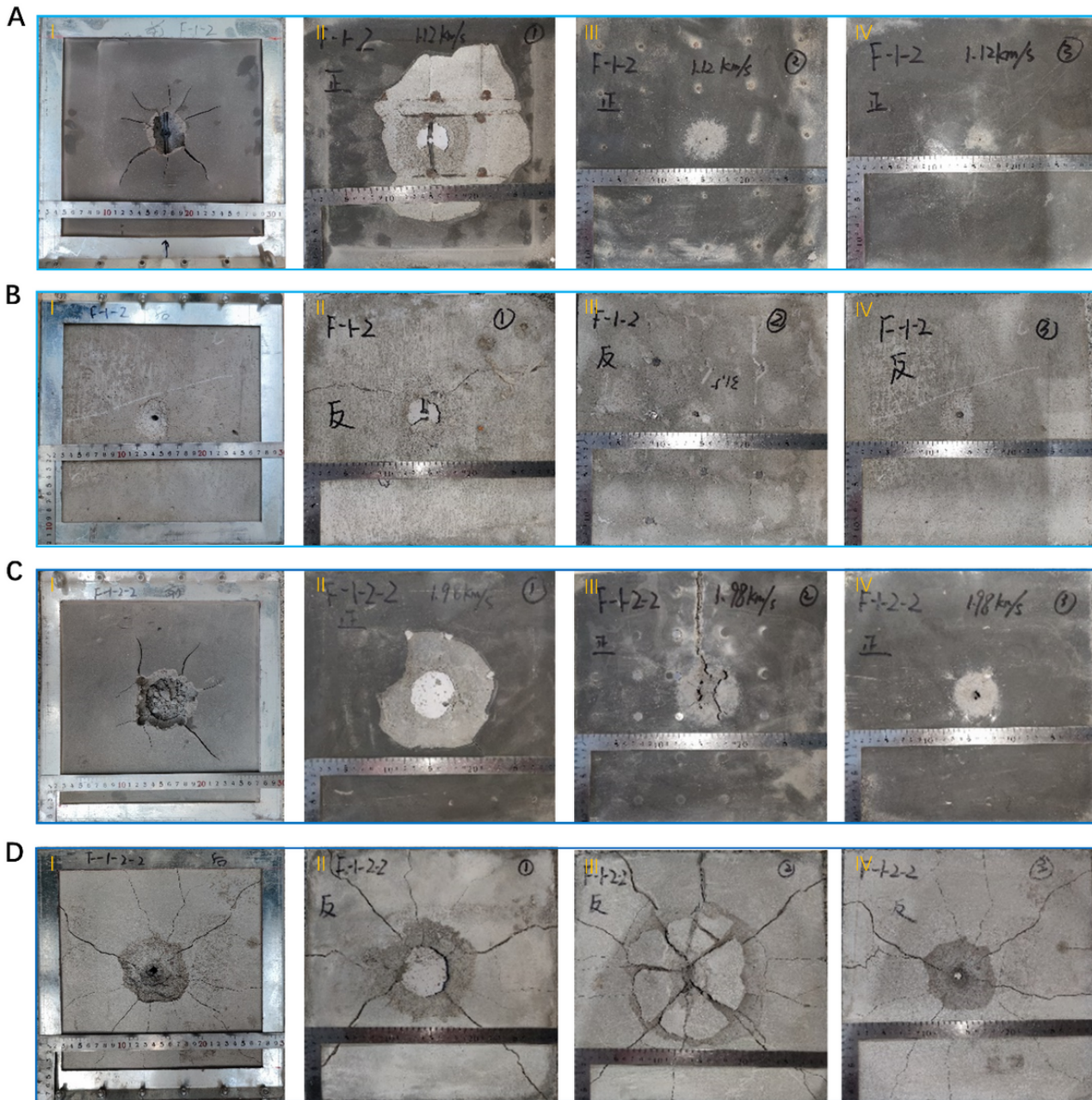


Figure 4

The observation of damage morphologies of the typical NISC-100 targets with different assembled layers, after the hypervelocity impact tests on the concrete targets under different striking velocities ($v = 1 \text{ km/s}$, 2 km/s). (A) Morphologies of frontal damage of the NISC target after the impact test under a striking velocity of 1 km/s . (B) Morphologies of the back damage of the NISC target after the impact test under a striking velocity of 1 km/s . (C) Morphologies of the frontal damage of the NISC target after the impact under a striking velocity of 2 km/s . (D) Morphologies of the back damage of the NISC target after the impact under a striking velocity of 2 km/s . From the second column to the fourth column: the first layer, the second layer, and the third layer.

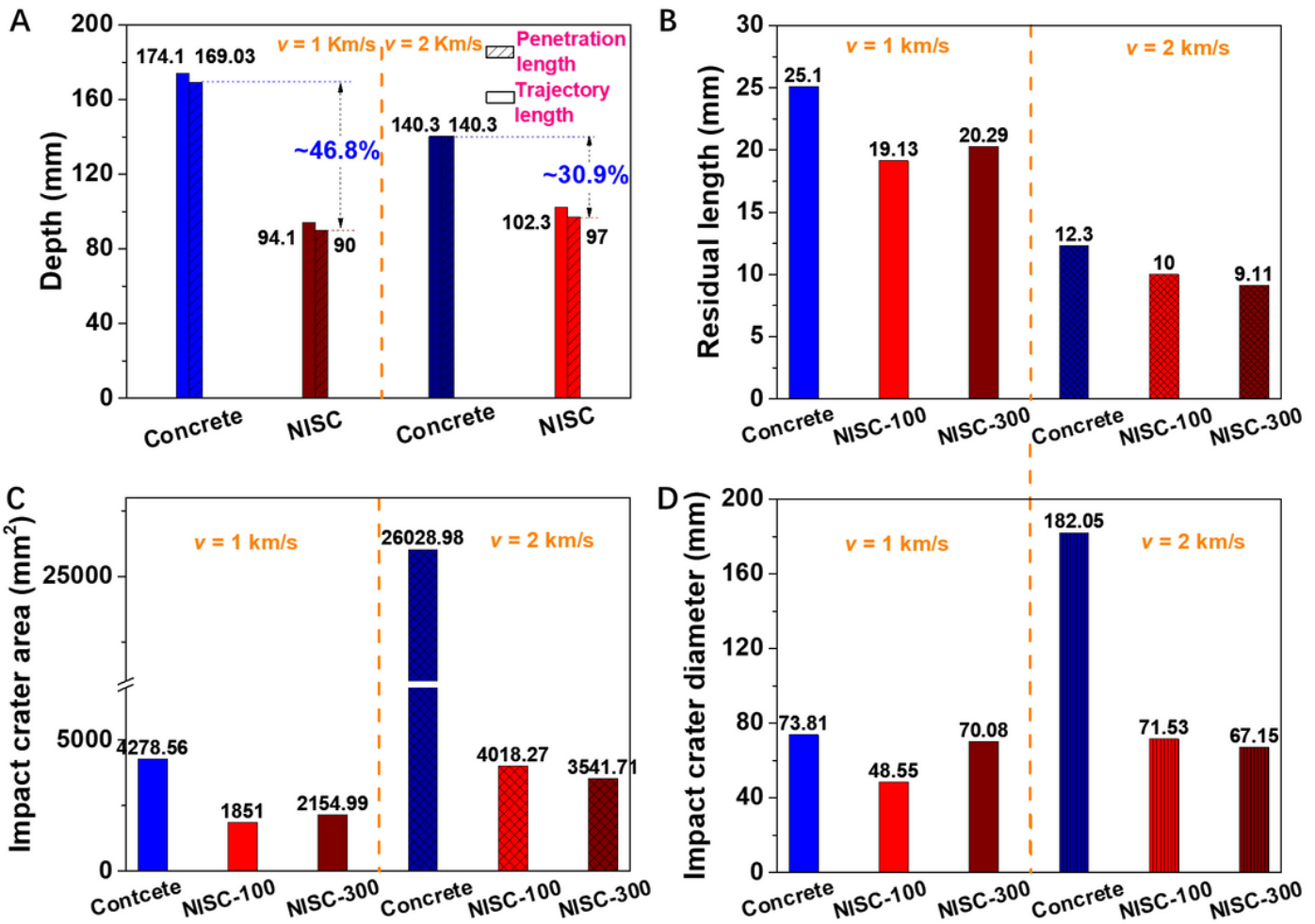


Figure 5

Comparison for ballistic performance of the typical NISC and pure concrete target under different striking velocities (1 km/s and 2 km/s). (A) Trajectory length and penetration depth of the pure concrete and the NISC. (B) Residual length of the projectile bodies. (C) Impact crater area of the pure concrete, NISC-100, and NISC-300 at their front sides. (D) Equivalent diameter of the impact crater of the pure concrete, NISC-100, and NISC-300 at their front sides.

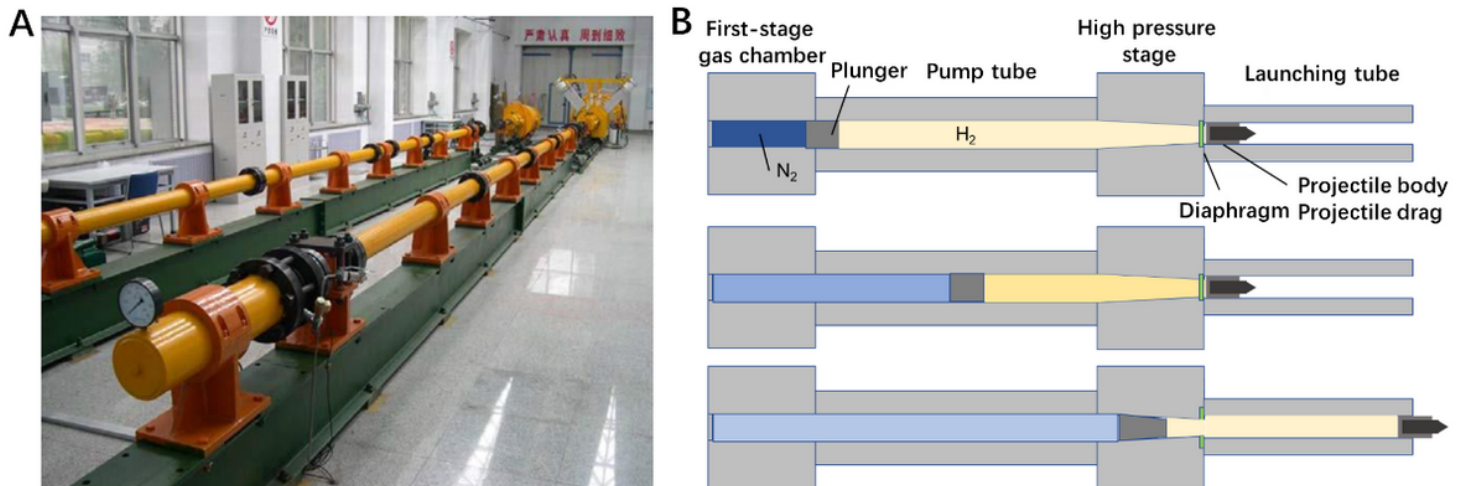


Figure 6

Photograph and working principle of the two-stage light-gas gun. (A) The two-stage light-gas gun system. (B) The working principle of the two-stage light-gas gun.

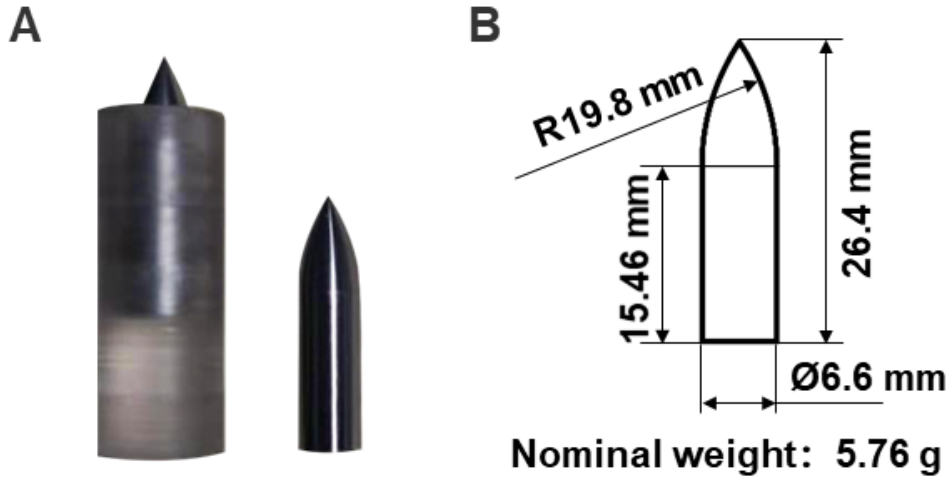


Figure 7

Photograph and dimension parameter of projectile with sabots used in the hypervelocity impact tests. (A) Photograph of the projectile with sabots. (B) The dimension parameter of the projectile.

Supplementary Files

This is a list of supplementary files associated with this preprint. Click to download.

- [MovieS1.avi](#)
- [MovieS2.avi](#)
- [MovieS3.avi](#)
- [NacrelikeSCcompositeSI.docx](#)